Experimental and theoretical study of the electronic states and spectra of PbLi

ARTICLE *in* JOURNAL OF MOLECULAR SPECTROSCOPY · SEPTEMBER 2002

Impact Factor: 1.48 · DOI: 10.1016/S0022-2852(02)00032-2

Available online at www.sciencedirect.com
SCIENCE DIRECT®
Journal of Molecular Spectroscopy 217 (2003) 127–141
Journal of MOLECULAR SPECTROSCOPY
www.elsevier.com/locate/jms

Experimental and theoretical study of the electronic states and spectra of PbLi

K.D. Setzer,[a] J. Borkowska-Burnecka,[a,1] W. Zyrnicki,[a,1] A.M. Pravilov,[a,2] E.H. Fink,[a,*] K.K. Das,[b,3] H.-P. Liebermann,[b] A.B. Alekseyev,[b,4] and R.J. Buenker[b]

[a] *Fachbereich 9, Physikalische Chemie, Bergische Universität Wuppertal, D-42097 Wuppertal, Germany*
[b] *Fachbereich 9, Theoretische Chemie, Bergische Universität Wuppertal, D-42097 Wuppertal, Germany*

Received 20 August 2002

Abstract

Gas phase emission spectra of the hitherto unknown free radical PbLi have been measured in the NIR range with a Fourier-transform spectrometer. The emissions were observed from a fast flow system in which lead vapor in argon carrier gas was passed through a microwave discharge and mixed with lithium vapor in an observation tube. Five electronic transitions have been found in the wavenumber range 3800–10 000 cm^{-1}. Bands from two excited states to the ground state were measured at high spectral resolution such that rotational analyses could be performed and accurate molecular parameters derived. In order to aid in the analysis of the experimental data, a series of relativistic configuration interaction calculations has been carried out to obtain potential curves for the low-lying states of PbLi and also electric dipole transition moments connecting them. As in the lighter molecules of this group, CLi and SiLi, the ground state of PbLi is found to be $X^4\Sigma^-(X_1\ 1/2, X_2\ 3/2)$ with a spin splitting of about 2000 cm^{-1}. The first excited state is $A^2\Pi_{1/2}$ (A 1/2), and two observed band systems are assigned to the transitions $A \rightarrow X_1$ and $A \rightarrow X_2$. Two more excited states, $B^2\Pi_{3/2}$ (B 3/2) and C 1/2, are identified from the observed spectra with the help of the computed data, and their spectroscopic constants are determined. In contrast to PbH and PbF, the ab initio results indicate a very complicated low-energy electronic structure for the PbLi radical, with 19 bound electronic states calculated to lie below 3 eV.

Keywords: Lead-lithium; Near-infrared transitions; Fourier-transform spectrometry; Relativistic calculations

1. Introduction

Whereas the monohydrides and monohalides of group IVa, Va, and VIa elements are known without exception and their electronic states and spectra have been the subject of numerous studies [1,2], most of the corresponding alkali compounds are still unknown. Recently, we have reported experimental and theoretical studies of the electronic spectra of BiNa [3] and TeLi [4], two representative alkali compounds of atoms of the latter two groups. As expected from the identical outer electronic configurations, the alkali compounds were found to have the same electronic ground states and low-lying excited states as the hydrides, but the relative positions of the states and the magnitude of the spin–orbit splitting were found to be distinctly different due to differences in bonding character (ionic vs. covalent) and relative MO energies.

In the present paper we report on experimental and theoretical studies of the electronic states and spectra of lead-lithium, PbLi, a radical representing the alkali compounds of group IVa atoms. As is known from theoretical studies of the lighter species consisting of first- and second-row atoms CLi, CNa, SiLi, and SiNa,

* Corresponding author. Fax: +49-202-439-2505.
E-mail address: fink@uni-wuppertal.de (E.H. Fink).
[1] Visiting Scientist from the Institute of Inorganic Chemistry and Metallurgy of Rare Elements, Technical University of Wroclaw, 50–370 Wroclaw, Poland.
[2] Visiting Scientist from the Institute of Physics, St. Petersburg State University, 198904 St. Petersburg, Russia.
[3] Present address: Physical Chemistry Section, Department of Chemistry, Jadavpur University, Calcutta 700 032, India.
[4] Present address: Institut für Physikalische und Theoretische Chemie, Universität Essen, Universitätsstrasse 5, D-45117 Essen, Germany.

0022-2852/02/$ - see front matter © 2002 Elsevier Science (USA). All rights reserved.
PII: S0022-2852(02)00032-2

in this group different bonding leads to the peculiarity that the lowest states are $^4\Sigma^-$ in character in contrast to CH and SiH which have $^2\Pi$ ground states [5–11]. In order to predict electronic spectra, Ricca and Bauchlicher [10] have calculated the spectroscopic constants for all doublet and quartet states of CLi below about 30 000 cm^{-1}. The only bound–bound quartet transition predicted in this energy range is $(2)^4\Sigma^- – X^4\Sigma^-$ which should occur between 10 000 and 25 000 cm^{-1}. However, due to avoided crossings the $(2)^4\Sigma^-$ state has a very broad potential energy curve, and the large difference in r_e values between the two states results in the intensity being spread out over many vibrational transitions. Therefore, in spite of the calculated large Einstein A coefficient ($A_{ul} \approx 10^7\ s^{-1}$) the emission spectrum of this transition will consist of many weak $v'–v''$ bands extending over a large wavelength range, and hence will be difficult to be observed.

In the doublet manifold of CLi, Ricca and Bauschlicher [10] found a number of stable states. Allowed doublet transitions, however, will lie below 15 000 cm^{-1} in the near-infrared range, and since these authors did not calculate transition probabilities for the transitions it is difficult to predict which would be the most promising transition to search for in emission spectra. The lack of states with spin-allowed transitions to the ground state likely is the reason why no electronic spectra in the UV/VIS region have been observed for any of the group IVa-alkali molecules. Except for recent millimeter/submillimeter wave absorption measurements of pure rotational lines in the $X^4\Sigma^-$ ground state of potassium carbide, KC [12], to the best of our knowledge, no experimental spectroscopic studies of any other molecule of the group IVa-alkali compounds have been reported.

As is well known, in molecules containing heavy fourth- or fifth-row atoms angular momentum coupling approaches Hund's case (c) and the electronic states show large spin–orbit splitting. The Λ–S states split into well-separated Ω states, and due to the absence of the spin selection rule more transitions become allowed. Also, in heavier molecules the excited states usually come down in energy so that electronic transitions show up in the near-infrared region between 0.7 and 4 μm which is well suited for emission measurements using low-background chemiluminescence sources and a Fourier-transform spectrometer equipped with sensitive Ge or InSb detectors. In continuation of our recent work on BiNa and TeLi, we have used this technique to study spectra of diatomic lead-alkali compounds. We readily have observed a number of transitions of PbLi, PbNa, and PbK. In the present paper we report on observation of five transitions of PbLi, two of which could be measured at high spectral resolution such that rotational analyses could be performed. In order to aid in the analysis of the experimental data and to identify the electronic states involved, a series of relativistic configuration interaction calculations has been carried out to obtain potential curves for the low-lying states of PbLi and also electric dipole transition moments connecting them.

The results of the analyses represent the first information about electronic spectra of a group IVa-alkali diatomic as yet reported.

2. Experimental details

As in previous work [3,4], the source of the emission spectra was a fast-flow system made of stainless steel and quartz tubes. A flow of Ar carrier gas was passed over molten lead metal in a ceramic boat heated to about 900 °C in a quartz tube, and the Pb_x vapor/Ar mixture was passed through a microwave discharge before entering a stainless steel observation tube of 1.2 m length and 4 cm diameter. From the opposite side, lithium vapor (Li_x) in Ar carrier gas was added to the afterglow of the Pb_x/Ar discharge. The lithium metal was heated to about 650 °C in a small stainless steel container. The tube was pumped with a 500 $m^3\,h^{-1}$ roots pump in series with a 40 $m^3\,h^{-1}$ forepump. The gas mixture of 100–200 Pa total pressure consisted of nearly equal flows of Ar carrier gas with traces of the metal vapors. The emission spectra were observed along the axis of the tube and were measured with a high-resolution Fourier-transform spectrometer (Bruker IFS 120 HR) equipped with a liquid-nitrogen-cooled Ge (Applied Detector, Model 403 S) or InSb (Cincinnati Electronics, Model IDH 100) detector. The wavenumber scale of the spectrometer was calibrated by use of emission lines of argon as standards [13]. The absolute accuracy of the measurements is thought to be better than 0.01 cm^{-1} and the relative precision of the wavenumbers of strong lines is of the order of 10^{-4} cm^{-1}.

3. Experimental results and analyses

Fig. 1 shows a survey spectrum recorded in the range 3600–6500 cm^{-1} at a resolution of 1 cm^{-1} with the less sensitive InSb detector. The spectrum was calculated from a coaddition of 305 interferograms recorded in about 30 min. It is free of atomic lines, showing that the microwave discharge did not extend into the observation tube. Four molecular emissions are observed. The weak feature at 5310 cm^{-1} is identified to be the $\Delta v = 0$ sequence of the recently detected fine structure transition of Pb_2 [14]. The other emissions are assigned to transitions of PbLi with the help of the results of the theoretical calculations reported below. The strong emission near 6059 cm^{-1} is attributed to the $\Delta v = 0$ sequence of the transition from the lowest excited $\Omega = 1/2$ state,

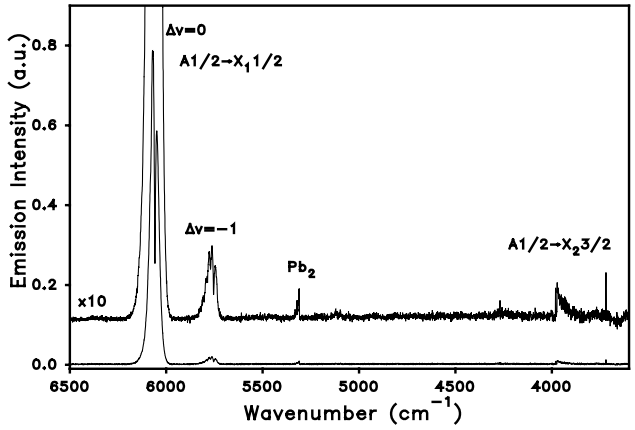

Fig. 1. Survey spectrum of the chemiluminescence in the range 3600–6500 cm^{-1} measured with the InSb detector. The spectral resolution is 1 cm^{-1}.

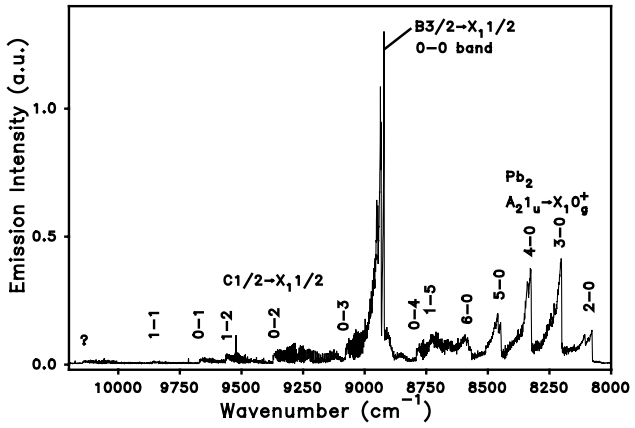

Fig. 2. Survey spectrum of the chemiluminescence in the range 8000–10 200 cm^{-1} measured with the Ge detector and a 8000 cm^{-1} long-pass filter. The spectral resolution is 0.5 cm^{-1}.

Table 1
Wavenumbers and observed–calculated differences for the bandheads of the $B\ 3/2 \rightarrow X_1\ 1/2$ system of $^{208}Pb^7Li$

v'–v''	$\tilde{\nu}$ (cm^{-1})
0–0	[9974.1][a]
0–1	9670.4(2)[b]
0–2	9371.5(−1)
0–3	9078.2(−1)
0–4	8790.3(0)
1–0	[10166.4]
1–1	9862.3(−2)
1–2	9564.1(2)

[a] Numbers in brackets are calculated wavenumbers.
[b] Numbers in parentheses are the observed–calculated differences in units of the last digit.

$A\ 1/2$, to the $\Omega = 1/2$ component of the $^4\Sigma^-$ ground state, X_1 1/2. In this wavenumber range, strong bands likewise show up in the spectra of PbNa and PbK, suggesting that the $A\ 1/2 \rightarrow X_1\ 1/2$ transitions are the most prominent features in the spectra of all Pb-alkali

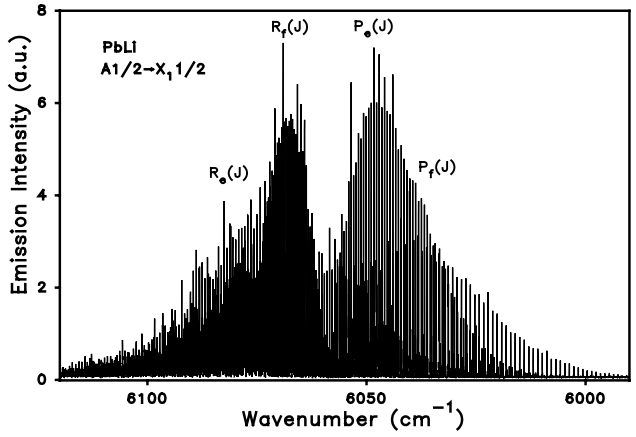

Fig. 3. High-resolution spectrum of the $\Delta v = 0$ sequence of the $A\ 1/2 \rightarrow X_1\ 1/2$ transition of PbLi. The line half-width is 0.024 cm^{-1}.

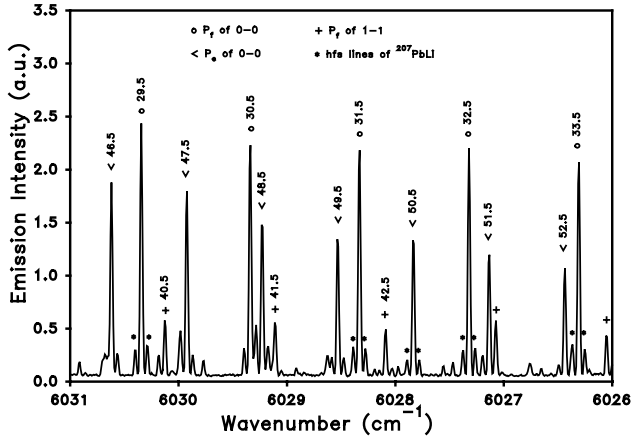

Fig. 4. Section of the $\Delta v = 0$ sequence of the $A\ 1/2 \rightarrow X_1\ 1/2$ transition of PbLi with line assignments. Some of the hfs lines of $^{207}Pb^7Li$ are marked with stars.

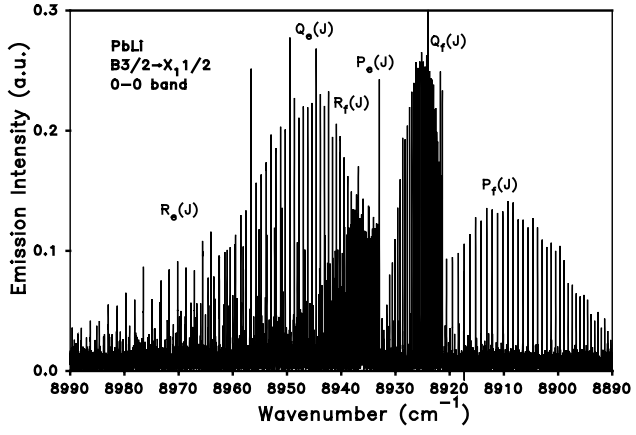

Fig. 5. High-resolution spectrum of the $\Delta v = 0$ sequence of the $B\ 3/2 \rightarrow X_1\ 1/2$ transition of PbLi. The line half-width is 0.024 cm^{-1}.

compounds. The nearby weaker feature at 5755 cm^{-1} is attributed to the $\Delta v = -1$ sequence of this transition. From the separation of the minima in the centers of the

Table 2
Rotational assignments and vacuum wavenumbers for lines in the 0–0 band of the $A\ 1/2 \rightarrow X_1\ 1/2$ transition of $^{208}Pb^7Li$ (in cm^{-1})

J	R_f	R_e	P_f	P_e
.5	6059.6880(−8)	6059.2996(−32)[b]		
1.5	6060.1610(−23)	6060.1610(130)[b]	6056.7401(106)[b]	6058.2279(0)
2.5	6060.6313(−1)	6060.9870(1)	6055.8596(1)	6057.7286(1)
3.5	6061.0931(−1)	6061.8233(39)[b]	6054.9830(−5)	6057.2365(136)[b]
4.5	6061.5486(0)	6062.6463(7)	6054.0985(−29)	6056.7113(2)
5.5	6061.9973(−3)	6063.4658(4)	6053.2134(0)	6056.1934(2)
6.5	6062.4412(8)	6064.2794(8)	6052.3198(2)	6055.6714(23)
7.5	6062.8766(−3)	6065.0852(−3)	6051.4197(−2)	6055.1394(3)
8.5	6063.3066(−4)	6065.8862(4)	6050.5146(0)	6054.6033(2)
9.5	6063.7290(−17)	6066.6798(2)	6049.6027(−10)	6054.0620(8)
10.5	6064.1499(17)	6067.4667(−1)	6048.6867(−4)	6053.5140(6)
11.5	6064.5582(−11)	6068.2476(1)	6047.7644(−7)	6052.9598(1)
12.5	6064.9640(−2)	6069.0149(−67)[b]	6046.8375(−2)	6052.4005(2)
13.5	6065.3624(−4)	6069.7885(−6)	6045.9135(84)[b]	6051.8358(6)
14.5	6065.7558(7)	6070.5518(17)	6044.9682(9)	6051.2646(1)
15.5	6066.1409(−5)	6071.3051(6)	6044.0319(75)[b]	6050.6882(−1)
16.5	6066.5208(−5)	6072.0541(18)	6043.0761(−4)	6050.1067(2)
17.5	6066.8944(−8)	6072.7938(2)	6042.1240(2)	6049.5196(2)
18.5	6067.2626(−4)	6073.5285(1)	6041.1658(−5)	6048.9272(3)
19.5	6067.6245(−2)	6074.2573(8)	6040.2056(14)	6048.3288(−5)
20.5	6067.9805(1)	6074.9789(6)	6039.2370(−5)	6047.7263(−2)
21.5	6068.3297(−5)	6075.6937(2)	6038.2663(−1)	6047.1178(−9)
22.5	6068.6736(−5)	6076.4003(−20)	6037.2909(−3)	6046.5058(−1)
23.5	6069.0149(28)	6077.1065(19)	6036.3115(−2)	6045.8896(13)
24.5	6069.3439(−4)	6077.8004(−1)	6035.3280(−3)	6045.2658(−2)
25.5	6069.6710(1)	6078.4902(1)	6034.3406(−3)	6044.6389(−2)
26.5	6069.9917(−1)	6079.1739(6)	6033.3488(−10)	6044.0090(14)
27.5	6070.3072(1)	6079.8503(1)	6032.3551(1)	6043.3715(−2)
28.5	6070.6166(−3)	6080.5209(0)	6031.3568(−1)	6042.7314(−1)
29.5	6070.9224(11)	6081.1849(−7)	6030.3556(1)	6042.0869(−3)
30.5	6071.2209(6)	6081.8438(−1)	6029.3510(1)	6041.4386(−2)
31.5	6071.5139(−3)	6082.4940(−24)	6028.3437(4)	6040.7864(−2)
32.5	6071.8033(5)	6083.1427(0)	6027.3328(−1)	6040.1305(0)
33.5	6072.0853(−10)	6083.7819(−11)	6026.3205(7)	6039.4705(−3)
34.5	6072.3650(1)	6084.4176(0)	6025.3047(4)	6038.8075(−1)
35.5	6072.6379(−7)	6085.0466(3)	6024.2869(6)	6038.1409(−2)
36.5	6072.9074(−2)	6085.6686(−8)	6023.2667(4)	6037.4715(2)
37.5	6073.1731(13)	6086.2900(33)[b]	6022.2462(20)	6036.7979(−6)
38.5	6073.4328(13)	6086.8984(−1)	6021.2207(4)	6036.1220(−7)
39.5	6073.6868(0)	6087.5021(−26)	6020.1950(2)	6035.4439(−3)
40.5	6073.9383(6)	6088.1055(−2)	6019.1679(1)	6034.7629(−2)
41.5	6074.1840(−4)	6088.7019(6)	6018.1396(−1)	6034.0795(−1)
42.5	6074.4271(1)	6089.2923(7)	6017.1105(0)	6033.3943(6)
43.5	6074.6648(−9)	6089.8754(−14)	6016.0800(−4)	6032.7050(−8)
44.5	6074.9004(0)	6090.4566(−5)	6015.0493(−4)	6032.0156(−3)
45.5	6075.1313(−2)	6091.0332(7)	6014.0180(−5)	6031.3250(7)
46.5	6075.3575(−16)	6091.6042(13)	6012.9859(−11)	6030.6310(0)
47.5	6075.5858(26)	6092.1703(14)	6011.9539(−16)[c]	6029.9359(−4)
48.5	6075.8040(0)	6092.7304(3)	6010.9223(−19)[c]	6029.2405(0)
49.5	6076.0204(−13)	6093.2884(15)	6009.8907(−26)[c]	6028.5439(3)
50.5	6076.2225(−139)[b]	6093.8444(50)[b]	6008.8599(−30)[c]	6027.8460(1)
51.5	6076.4462(−21)[c]	6094.3851(−26)[c]	6007.8299(−35)[c]	6027.1476(0)
52.5	6076.6538(−37)[c]	6094.9269(−51)[c]	6006.8003(−48)[c]	6026.4489(2)
53.5	6076.8562(−79)[c]	6095.4735(13)[c]	6005.7724(−55)[c]	6025.7500(3)
54.5	6077.0584(−101)[c,b]	6096.0111(24)[c]	6004.7448(−74)[c]	6025.0488(−18)[c]
55.5	6077.2631(−75)[c]	6096.5422(7)[c]	6003.7203(−81)[c]	6024.3500(−16)[c]
56.5	6077.4614(−93)[c]	6097.0755(48)[c]	6002.6966(−99)[c]	6023.6530(1)
57.5	6077.6528(−161)[c,b]	6097.5978(13)[c]	6001.6759(−109)[c]	6022.9550(0)
58.5	6077.8589(−66)[c]	6098.1196(5)	6000.6573(−123)[c]	6022.2462(−116)[c,b]
59.5	6078.0559(−47)[c]	6098.6378(−8)	5999.6411(−140)[c]	6021.5624(8)[c]
60.5	6078.2579(36)[c]	6099.1591(39)[c]	5998.6276(−159)[c]	6020.8668(1)[c]
61.5	6078.4390(−78)[c]	6099.6713(23)[c]	5997.6159(−193)[c]	6020.1689(−44)[c]
62.5	6078.6513(127)[c,b]	6100.1819(18)[c]	5996.6090(−214)[c]	6019.4816(1)[c]

Table 2 (*continued*)

J	R_f	R_e	P_f	P_e
63.5	6078.8350(55)[c,b]	6100.7002(113)[c,b]	5995.6078(−215)[c]	6018.7916(0)[c]
64.5	6079.0335(137)[c,b]	6101.1982(29)[c]	5994.6061(−261)[c]	6018.1043(4)[c]
65.5	6079.2098[a]	6101.6927(−68)[c]	5993.6126(−268)[c]	6017.4172(−14)[c]
66.5	6079.3996[a]	6102.2017(−2)[c]	5992.6191(−319)[c]	6016.7351(−8)[c]
67.5	6079.5999(104)[c,b]	6102.7040(16)[c]	5991.6329(−347)[c]	6016.0521(−40)[c]
68.5	6079.7796[a]	6103.1943(−71)[c]	5990.6484(−407)[c]	6015.3775(−19)[c]
69.5	6079.9702[a]	6103.6921(−68)[c]	5989.6779(−382)[c]	6014.7055(−7)[c]
70.5	6080.1614[a]	6104.2042(91)[c]	5988.7017(−469)[c]	6014.0463(97)[c,b]
71.5	6080.3535[a]	6104.6958(54)[c]	5987.7360(−510)[c]	6013.3670(−37)[c]
72.5	6080.5468[a]	6105.1788(−60)[c]	5986.7734(−583)[c]	6012.7062(−29)[c]
73.5	6080.7413[a]	6105.6803(18)[c]	5985.8828[a]	6012.0465(−53)[c]
74.5	6080.9374[a]	6106.1691(−26)[c]	5984.9407[a]	6011.3984(−8)[c]
75.5	6081.1352[a]	6106.6587(−60)[c]	5984.0057[a]	6010.7458(−57)[c]
76.5	6081.3351[a]	6107.1494(−82)[c]	5983.0780[a]	6010.1031(−59)[c]
77.5	6081.5372[a]	6107.6573(66)[c,b]	5982.1580[a]	6009.4612(−108)[c]
78.5	6081.7417[a]	6108.1347(−94)[c]	5981.2460[a]	6008.8326(−82)[c]
79.5	6081.9490[a]	6108.6322(−58)[c]	5980.3422[a]	6008.2101(−53)[c]
80.5	6082.1592[a]	6109.1257(−70)[c]	5979.4471[a]	6007.5965[a]

[a] Calculated line.
[b] Experimental line, not used because of overlapping.
[c] Experimental line, not used because of isotope splitting.

bands, $\Delta G_{1/2}$ in the X_1 1/2 state is estimated to be 304.5 cm^{-1}. The relative intensities of the two sequences show that the states involved have nearly parallel potential energy curves. The single weak band near 3972 cm^{-1} is assigned to the transition from the same upper state A 1/2 to the second component of the $^4\Sigma^-$ ground state, X_2 3/2. The fine structure splitting in the $X^4\Sigma^-$ ground state thus is found to be 2086.6±0.5 cm^{-1}. Accounting for the wavelength dependence of the sensitivity of the detection system, the ratio of the integrated intensities of the $\Delta v = 0$ sequences of the A 1/2 → X_1 1/2 and A 1/2 → X_2 3/2 transitions is estimated to be 150 ± 30.

Fig. 2 shows a survey spectrum in the range 8000–10 200 cm^{-1} measured at a resolution of 0.5 cm^{-1} with the Ge detector and a 8000 cm^{-1} long-pass filter. The blue-degraded bands between 8100 and 8600 cm^{-1} are identified to belong to the v', $v'' = 0$ progression of the $A_2 1_u \rightarrow X_1 0_g^+$ transition of Pb_2 [14]. The strong band at 8930 cm^{-1} is assigned to be the 0–0 band of the B 3/2 → X_1 1/2 transition of PbLi. The region around 8625 cm^{-1}, where the 0–1 band of this transition should show up, is congested by other bands, but the intensity of the 0–1 band is clearly lower by a factor of 20 than that of 0–0, showing that the potential energy curve of the B 3/2 state also must be nearly parallel to that of the X_1 1/2 ground state. By contrast, the fourth transition, denoted C 1/2 → X_1 1/2, consists of a number of weak red-degraded bands in the range 8500–9700 cm^{-1}. The maximum intensity in the $v' = 0$, v'' progression occurs near $v'' = 3$, suggesting that the potential curve of the C 1/2 state is shifted to larger r_e values. Four bands of the $v' = 0$, v'' and two bands of the $v' = 1$, v'' progressions were assigned, and from analysis of the wavenumbers of the bandheads (Table 1) the following data for the X_1 1/2 and C 1/2 states were obtained (in cm^{-1}): X_1 1/2: $\omega_e = 309.2(7)$, $\omega_e x_e = 2.65(11)$; C 1/2 : $T_0 = 9974.1(6)$, $\Delta G_{1/2} = 192.3(3)$, where the numbers in parentheses are the standard deviations of the fitted parameters. For the X_1 1/2 ground state, $\Delta G_{1/2} = 303.9\,cm^{-1}$ is obtained in good agreement with the value estimated above from the separation of the 0–0 and 0–1 bands of the A 1/2 → X_1 1/2 transition. Two other weak red-degraded bands with heads at 10146.0 and 10748.5 cm^{-1} could not yet be assigned. A search was made for bands of the B 3/2 → X_2 3/2 and C 1/2 → X_2 3/2 transitions, but the wavenumber ranges where these transitions are calculated to occur are heavily congested by Pb_2 bands. A sharp peak observed at 6852.1 cm^{-1} is identified to be the R-branch head of the 0–0 band of the B 3/2 → X_2 3/2 transition (see below), but no bands of the C 1/2 → X_2 3/2 transition could be identified. It is estimated that the intensities of these transitions are at least a factor of 10 lower than those of the transitions to the X_1 1/2 state.

The strong $\Delta v = 0$ sequences of the $A \rightarrow X_1$ and $B \rightarrow X_1$ transitions have been measured at high resolution with linewidths of about 0.02 cm^{-1}. Fig. 3 shows a spectrum of the A 1/2 → X_1 1/2 emission near 6050 cm^{-1} which is a superposition of a strong 0–0 band and an approximately three times weaker 1–1 band. Due to Ω-doubling in both $\Omega = 1/2$ states, the bands consist of two R and P branches each. The 1–1 band is shifted to higher wavenumbers, showing that the vibrational spacing in the A state is larger by about 10 cm^{-1} than in the X_1 state. Fig. 4 shows a section of the P-branch region with some line assignments. Natural lead consists of four stable isotopes, ^{204}Pb, ^{206}Pb, ^{207}Pb, and ^{208}Pb, with relative

abundances of 1.4, 24.1, 22.1, and 52.4%. ^{207}Pb has a nuclear spin of $I = 1/2$. Lithium has two stable isotopes with abundances of 7.4% (^{6}Li) and 92.6% (^{7}Li) and spins of $I = 1$ and $I = 3/2$, respectively. The three most abundant isotopic species ^{208}Pb^{7}Li (48.5%), ^{206}Pb^{7}Li (22.3%), and ^{207}Pb^{7}Li (20.5%) should show up in the spectra. Due to the small difference of the vibrational quanta in the A and X_1 states of about 10 cm^{-1}, the vibrational isotope shift for the 0–0 and 1–1 bands is less than the linewidth and can be neglected. The rotational isotope effect due to the lead isotopes likewise is weak and shows up as broadening of the lines at high J values. As is seen from Fig. 4, as in the spectra of the previously studied PbF [15] and PbH [16] molecules, all strong lines are accompanied by two approximately 10 times weaker symmetric satellite lines which are assigned to magnetic hyperfine structure transitions of ^{207}Pb^{7}Li. For large J values, the width of the splitting is approximately equal to the product of the splitting parameter d and the nuclear spin $I = 1/2$ of ^{207}Pb, $\Delta\nu = dI$ [17]. From the average splitting of 0.122 cm^{-1}, $d = 0.244$ cm^{-1} is obtained.

A high-resolution spectrum of the 0–0 and 1–1 bands of the $B\ 3/2 \rightarrow X_1\ 1/2$ transition is shown in Fig. 5. The bands consist of two R, Q, and P branches each, with two branches of the strong 0–0 band forming heads at 8932.97 and 8921.35 cm^{-1}. The 1–1 band is about a factor of 4 lower in intensity and again is shifted by $\approx$12 cm^{-1} to higher wavenumbers. Different from the $A \rightarrow X_1$ band, no satellite lines show up on both sides of the strong lines showing that the hfs splitting is a characteristic of the A 1/2 but not of the X_1 1/2 state.

The bands were analyzed as transitions between $\Omega = 1/2$ and $\Omega = 3/2$ states (Hund's case (c) limit) using the same formalism as in the work of Lumley and Barrow on PbF [18]. For the X_1 1/2 and A 1/2 states the rotational term values were calculated as

$$F_f(J) + F_e(J) = 2[T_0 + BJ(J+1) - DJ^2(J+1)^2 + HJ^3(J+1)^3], \quad (1)$$

$$F_f(J) - F_e(J) = p_{1/2}(J+1/2) + p_D(J+1/2)^3 \quad (2)$$

and for B 3/2 Eqs. (1) and (3) were used,

$$F_f(J) - F_e(J) = p_{3/2}(J+1/2)(J-1/2)(J+3/2). \quad (3)$$

The e and f labelling of the rotational levels was chosen such that in all states $F_e(J) < F_f(J)$, corresponding to positive values of $p_{1/2}$ and $p_{3/2}$. Vacuum wavenumbers of the lines of the 0–0 bands of the $A \rightarrow X_1$ and $B \rightarrow X_1$ transitions of ^{208}Pb^{7}Li and the observed–calculated differences are given in Tables 2 and 3. In some branches of the 0–0 band of the $A \rightarrow X_1$ transition, the line series could be followed up to $J = 80.5$, but for $J > 50$ systematic, mostly negative deviations of the experimental and calculated wavenumbers were observed (Table 2). These deviations are attributed to rotational isotope splitting of the lines of ^{208}Pb^{7}Li and ^{206}Pb^{7}Li which are superimposed for low J values. Therefore, most high-J lines were not used in the least-squares fit. The results of the fits are shown in Table 4. The Ω-doubling in the B 3/2 state was found to be negligible, $p_{3/2}$ was not well determined and therefore was set to 0 in the final fits. The parameters of the $v = 0$ and 1 states were used to calculate the equilibrium parameters given in Table 5.

In order to confirm the assignment of the weak $A\ 1/2 \rightarrow X_2\ 3/2$ band at 3972 cm^{-1}, the shape of this band was compared with a simulated band contour (Fig. 6). For the A 1/2, $v' = 0$ state the rotational constants obtained from the analysis of the 0–0 band of the $A \rightarrow X_1$ transition were used (Table 4), and the B_0 value of X_2 3/2 was estimated by correcting $B_0(X_1)$ with the ratio of the squares of the equilibrium internuclear distances in the X_1 and X_2 states obtained in the theoretical calculations (see below), $B_0(X_2) = B_0(X_1) r_e(X_1)^2 / r_e(X_2)^2$. Using $T_0(X_2) = 2086.6$ cm^{-1}, $B_0(X_2) = 0.367$ cm^{-1}, $D_0(X_2) \approx D_0(X_1)$, and $T = 400$ K the simulated band contour shows reasonable agreement with the experimental bandshape (Fig. 6), thus confirming the assignment. In Fig. 7, the experimental spectrum near 6850 cm^{-1} is shown together with a simulation of the 0–0 band of the $B\ 3/2 \rightarrow X_2\ 3/2$ transition performed using the same parameters for the $v = 0$ level of the X_2 state and the B, $v = 0$ data from Table 4. The form of the band with the sharp R-branch head and the agreement of the peak positions also strongly support the assignments.

The $C\ 1/2 \rightarrow X_1\ 1/2$ bands are rather weak and could be measured at a resolution of only 0.1 cm^{-1}. Due to Ω-doubling in the upper and lower states they should consist of two R and P branches each. A closer look at the bands revealed strong perturbations at intermediate J levels showing up by line shifts, irregular line intensities, and the appearance of weak Q-branch lines. Fig. 8 shows a comparison of a section of the 0–2 band (upper trace) with a rough simulation of the band (lower trace) obtained by using rotational constants of the X_1 1/2, $v'' = 2$ state calculated from the data in Table 5, a rotational constant of the C 1/2, $v' = 0$ state estimated from $B_0(X_1)$ and the calculated internuclear distances by $B_0(C) = B_0(X_1)\ r_e(X_1)^2 / r_e(C)^2$, and adjusting the position of the bandhead and the value of the Ω-doubling parameter in the C state ($p' = 0.618$ cm^{-1}). The rough agreement of the bandshapes supports the theoretical r_e value of the C 1/2 state. Spectra with higher resolution and better signal-to-noise ratios are needed for detailed analysis of the bands.

4. Theoretical calculations

In order to facilitate the analysis of the present experimental spectra, a series of ab initio relativistic configuration interaction (CI) calculations have been carried out for the PbLi radical. For this purpose, a

Table 3
Rotational assignments and vacuum wavenumbers for lines in the 0–0 band of the $B\ 3/2 \rightarrow X_1\ 1/2$ transition of $^{208}Pb^{7}Li$ (in cm^{-1})

J	R_e	Q_e	P_e	R_f	Q_f	P_e
1.5	8936.1104[a]	8934.3903[a]	8933.3582[a]	8933.8536(−17)	8932.1352[a]	8931.1031[a]
2.5	8937.3936[a]	8934.9856[a]	8933.2655[a]	8934.0083(−28)	8931.6037(6)	8929.8830[a]
3.5	8938.6868(−24)	8935.5933[a]	8933.1854[a]	8934.1776(−18)	8931.0837(0)	8928.6757[a]
4.5	8939.9952(−17)	8936.2136[a]	8933.1178[a]	8934.3607(2)	8930.5776(5)	8927.4813[a]
5.5	8941.3171(1)	8936.8457(−5)	8933.0629[a]	8934.5547(6)	8930.0828(−5)	8926.3000[a]
6.5	8942.6464(−28)	8937.4901(−12)	8933.0205[a]	8934.7595(−9)	8929.6012(−13)	8925.1302(−15)
7.5	8943.9925(−10)	8938.1490(2)	8932.9908[a]	8934.9801(7)	8929.1349(3)	8923.9767[a]
8.5	8945.3527(29)	8938.8193(8)	8932.9737[a]	8935.2093(−17)	8928.6792(−5)	8922.8365(15)
9.5	8946.7177(−4)	8939.5005(−1)	8932.9693[a]	8935.4552(−1)	8928.2384(6)	8921.7065[a]
10.5	8948.1003(21)	8940.1960(10)	8932.9775[a]	8935.7091(−32)	8927.8091(1)	8920.5900(−16)
11.5	8949.4902[a]	8940.9027(12)	8932.9968(−16)	8935.9841(21)	8927.3933(−1)	8919.4899(−3)
12.5	8950.8937(−1)	8941.6207(3)	8933.0295(−24)	8936.2640(−5)	8926.9913(3)	8918.4016(−8)
13.5	8952.3094(2)	8942.3533(18)	8933.0769(−11)	8936.5617(21)	8926.6020(2)	8917.3290(6)
14.5	8953.7365(2)	8943.0960(13)	8933.1355(−14)	8936.8676[a]	8926.2264(4)	8916.2682(1)
15.5	8955.1750(1)	8943.8523(22)	8933.2078(−7)	8937.1883[a]	8925.8640(5)	8915.2216(−4)
16.5	8956.6268(18)	8944.6209(33)	8933.2917(−11)	8937.5218(0)	8925.5152(7)	8914.1899(2)
17.5	8958.0859(−6)	8945.3989(17)	8933.3874(−24)	8937.8678(−5)	8925.1788(−1)	8913.1704(−10)
18.5	8959.5602(7)	8946.1907(17)	8933.5016(19)	8938.2274(−1)	8924.8573(4)	8912.1671(−6)
19.5	8961.0410(−27)	8946.9935(7)	8933.6232(9)	8938.6009(13)	8924.5499(13)	8911.1772(−9)
20.5	8962.5382(−11)	8947.8093(7)	8933.7586(10)	8938.9853(7)	8924.2545(5)	8910.2026(−4)
21.5	8964.0448(−13)	8948.6380(15)	8933.9075(17)	8939.3845(19)	8923.9738(8)	8909.2409(−15)
22.5	8965.5626(−15)	8949.4765[a]	8934.0671(1)	8939.7944(8)	8923.7065(5)	8908.2965(1)
23.5	8967.0920(−11)	8950.3302(17)	8934.2415(6)	8940.2179(5)	8923.4534(6)	8907.3654(1)
24.5	8968.6310(−23)	8951.1927(2)	8934.4293(16)	8940.6557(13)	8923.2140(5)	8906.4487(−2)
25.5	8970.1845[a]	8952.0707(23)	8934.6302(27)	8941.1070(26)	8922.9885(1)	8905.5487(12)
26.5	8971.7480(14)	8952.9565(1)	8934.8406(4)	8941.5700(25)	8922.7773(1)	8904.6608(−4)
27.5	8973.3197[a]	8953.8566(4)	8935.0657(−2)	8942.0460(22)	8922.5805(2)	8903.7909(9)
28.5	8974.9005(−32)	8954.7696(15)	8935.3042(−4)	8942.5352(21)	8922.3976(0)	8902.9345(4)
29.5	8976.4953(−32)	8955.6930(11)	8935.5574(10)	8943.0361(4)	8922.2292(0)	8902.0934(−2)
30.5	8978.1003(−37)	8956.6268(−9)	8935.8212(0)	8943.5533(18)	8922.0743(−9)	8901.2682(−6)
31.5	8979.7178(−26)	8957.5780(26)	8936.0991[a]	8944.0806[a]	8921.9351(−6)	8900.4582(−12)
32.5	8981.3474[a]	8958.5360(9)	8936.3902[a]	8944.6209(−21)	8921.8098(−9)	8899.6659(1)
33.5	8982.9850[a]	8959.5040(−26)	8936.6944[a]	8945.1804(17)	8921.7003[a]	8898.8878(−2)
34.5	8984.6298(−35)	8960.4887(−15)	8937.0123(4)	8945.7465(−14)	8921.6028(−19)	8898.1245(−18)
35.5	8986.2922[a]	8961.4861(5)	8937.3415(−10)	8946.3294(−10)	8921.5237(−1)	8897.3785(−21)
36.5	8987.9616[a]	8962.4929(−1)	8937.6874(10)	8946.9238(−25)	8921.4575(−2)	8896.6495(−17)
37.5	8989.6415[a]	8963.5136(14)	8938.0454(18)	8947.5366(8)	8921.4078(12)	8895.9367(−12)
38.5	8991.3313(−5)	8964.5436(2)	8938.4124(−18)	8948.1605(16)	8921.3721(16)	8895.2399(−13)
39.5	8993.0326[a]	8965.5865[a]	8938.7981[a]	8948.7959(4)	8921.3494[a]	8894.5596(−14)
40.5	8994.7437[a]	8966.6415[a]	8939.1958(4)	8949.4454(−4)	8921.3436[a]	8893.8981(6)
41.5	8996.4652[a]	8967.7084[a]	8939.6083(21)	8950.1112(15)	8921.3529[a]	8893.2508[a]
42.5	8998.1969[a]	8968.7873[a]	8940.0310(4)	8950.7873[a]	8921.3777[a]	8892.6205(−4)
43.5	8999.9389[a]	8969.8780[a]	8940.4682(−1)	8951.4782(−4)	8921.4178[a]	8892.0078(−4)
44.5	9001.6911[a]	8970.9807[a]	8940.9198[a]	8952.1838[a]	8921.4734[a]	8891.4115(−10)
45.5		8972.0952[a]	8941.3847[a]	8952.9029[a]	8921.5446[a]	8890.8342(1)
46.5		8973.2217[a]		8953.6358[a]	8921.6319(5)	8890.2731[a]
47.5		8974.3601[a]		8954.3826[a]	8921.7313(−27)	8889.7296[a]
48.5		8975.5104[a]		8955.1434[a]	8921.8524(1)	8889.2037[a]
49.5		8976.6726[a]		8955.9182[a]	8921.9890(24)	8888.6956[a]
50.5				8956.7071[a]	8922.1370(1)	8888.2053[a]
51.5					8922.3047(15)	
52.5					8922.4857[a]	

[a] Calculated line.

relativistic effective core potential (RECP) of Christiansen et al. [19] has been employed to describe the inner-shell electrons of the lead atom, so that only the 5*d*, 6*s*, and 6*p* electrons are treated explicitly in the calculations. The (5*s*5*p*6*d*) atomic orbital (AO) basis set for Pb optimized in [19] for use with the above RECP has been employed in the same [5*s*5*p*1*d*] contraction as in our recent PbF study [20]. The lithium 1*s* shell is also described by a RECP of the same shape-consistent type [21]. The (4*s*4*p*) basis set for Li [21] has been employed in uncontracted form and augmented by 1*p* ($0.005a_0^{-2}$) and 2*d* (0.20 and 0.07) functions.

Table 4
Results of least-squares fits of the $A\ 1/2 \rightarrow X_1\ 1/2$ and $B\ 3/2 \rightarrow X_1\ 1/2$ bands of $^{208}Pb^7Li$ (in cm^{-1})

Parameter	$A\ 1/2 \rightarrow X_1\ 1/2$		$B\ 3/2 \rightarrow X_1\ 1/2$	
	0–0	1–1	0–0	1–1
v_0	6058.4943(2)[a]	6069.0684(3)	8933.2391(2)	8947.0728(9)
B'	0.334619(4)	0.330705(5)	0.344038(6)	0.340368(27)
$10^5 D'$	0.1492(3)	0.1495(2)	0.1584(3)	0.155(3)
$10^{11} H'$	0.12(6)			
p'	0.7569(2)	0.7458(4)		
$10^5 p_{D'}$	−0.858(6)	−0.89(2)		
B''	0.337734(4)	0.333805(5)	0.337727(6)	0.333775(27)
$10^5 D''$	0.1640(3)	0.165(2)	0.1639(3)	0.164(3)
$10^{11} H''$	0.16(6)			
p''	1.1277(2)	1.1146(4)	1.12763(2)	1.11443(9)
$10^4 p_{D''}$	−0.1324(6)	−0.133(2)	−0.136(2)	−0.139(2)
N[b]	194	148	208	102
σ[c]	0.00085	0.0014	0.0014	0.0031

[a] Numbers in parentheses are the standard deviations of the parameters in units of the last digit.
[b] Number of lines fitted.
[c] Standard deviation of the fit.

Table 5
Molecular parameters of $^{208}Pb^7Li$ (in cm^{-1})[a]

Parameter	$X_1\ 1/2$	$X_2\ 3/2$	$A\ 1/2$	$B\ 3/2$	$C\ 1/2$
T_0	0	2086.6	6058.494	8933.239	9974.1
ω_e	309.2	(*354*)[b,c]	319.8[d]	323.0[d]	(195.7)
	309.2[c]		*319.6*[c]	*324.7*[c]	
$\omega_e x_e$	2.65		2.65[e]	2.65[e]	(1.7)
$\Delta G_{1/2}$	303.9		314.5	317.7	192.3
B_e	0.3397	(0.369)	0.33658	0.34587	(0.263)
α_B	−0.00394	(−0.00394)[e]	−0.00391	−0.00367	(−0.0039)
$10^6 (D_e \approx D_0)$	1.64	(1.64)[e]	1.49	1.57	(1.4)
p_e	1.1343		0.762		(0.625)
α_p	−0.0132		−0.011		(−0.013)[e]
$10^4 (p_{De} \approx p_{D0})$	−0.135		−0.086		(−0.08)
d			0.244		
r_e (Å)	2.70402		2.71653	2.6798	

[a] As many of the numbers are estimates, no error limits are given for the data in this table. Error limits for some parameters can be derived from the data in Table 4.
[b] Numbers in parentheses are rough estimates used for the simulation of band profiles.
[c] Numbers in italics are calculated by the Kratzer relation $\omega_e = (4B_e^3/D_e)^{1/2}$.
[d] Numbers estimated by $\omega_e = \Delta G_{1/2} + 2\omega_e x_e$.
[e] Fixed to the data for the $X_1\ 1/2$ state.

In the present study two different computational approaches are employed. In the first of them, a self-consistent field (SCF) calculation is combined with a large scale configuration interaction (CI) to obtain highly correlated Λ–S wavefunctions in the absence of spin–orbit coupling. As a next step a spin–orbit matrix for a relatively small number of Λ–S states ($\leqslant 100$) is diagonalized to obtain energies and wavefunctions for the final states, so that this approach may be characterized as a Λ–S contracted spin–orbit CI (LSC–SO–CI). As a more computationally demanding alternative to the above procedure, we have also performed calculations in which the electrostatic and spin–orbit interactions are treated simultaneously. In this case a larger secular equation is solved, in which all selected configurations of various space and spin symmetries form the basis for the multireference spin–orbit configuration interaction (MR–SO–CI) calculations, without first obtaining correlated Λ–S functions. More details for both methods employed may be found in our previous publications [22,23].

The first step in both computational schemes is to carry out an SCF calculation for the $^4\Sigma^-(\ldots\sigma\pi^2)$ state. Only the spin-independent part of the core potentials (AREPs) is employed at the SCF level as well as at the CI step of the LSC–SO–CI approach. All calculations are carried out formally in the C_{2v} subgroup, but the resulting MOs transform according to irreducible representations of the full $C_{\infty v}$ linear group, which is very helpful for the final analysis. The standard multirefer-

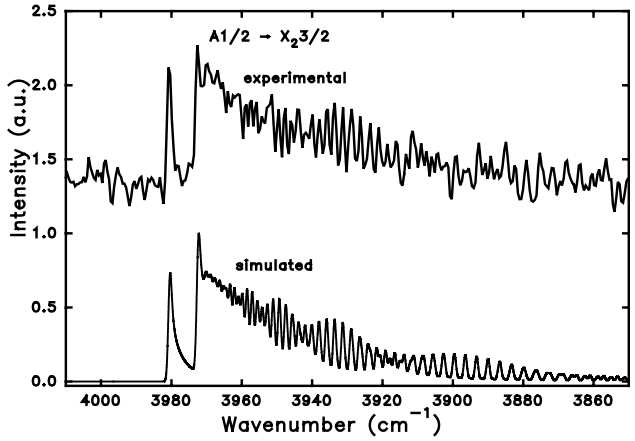

Fig. 6. Comparison of the weak 0–0 band of the $A\ 1/2 \rightarrow X_2\ 3/2$ of PbLi with a simulated band profile. The spectral resolution is $0.5\,\mathrm{cm}^{-1}$.

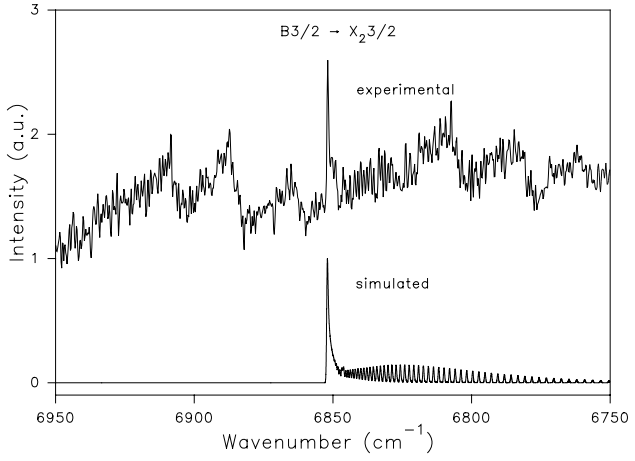

Fig. 7. Comparison of the experimental spectrum in the range 6750–6950 cm^{-1} with a simulated band profile of the 0–0 band of the $B\ 3/2 \rightarrow X_2\ 3/2$ transition. The spectral resolution is $0.5\,\mathrm{cm}^{-1}$.

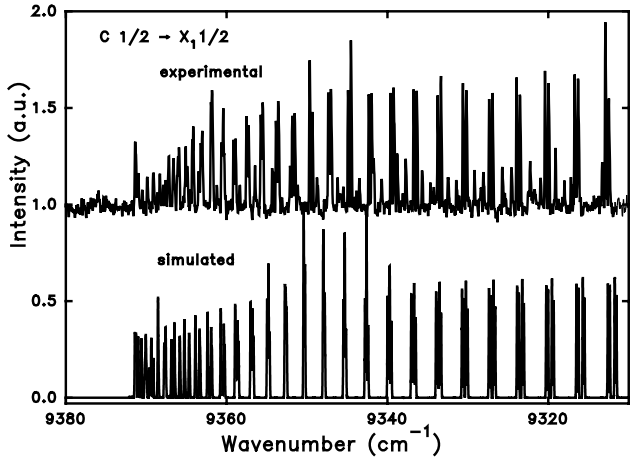

Fig. 8. Comparison of a section of the 0–2 band of the $C\ 1/2 \rightarrow X_1\ 1/2$ transition of PbLi with a simulated band profile. The spectral resolution is $0.1\,\mathrm{cm}^{-1}$.

ence single- and double-excitation CI method [24] is used to obtain the Λ–S electronic energies, wavefunctions and properties. The calculations have been carried out employing the Table Direct-CI [25,26] version of the MRD-CI package including configuration selection and perturbative corrections. Molecular orbitals (MOs), which are predominantly occupied by the lead $5d^{10}$ electrons, have been frozen at the CI stage of the calculations. In the LSC–SO–CI calculations, a selection threshold of $T = 0.05 \times 10^{-6} E_h$ has been used throughout. From 5 to 7 lowest roots have been calculated for each of all possible doublet and quartet irreducible representations and typical sizes of the selected CI spaces have been $(20\text{–}25) \times 10^3$ in each case. The importance of higher excitations in the LSC–SO–CI treatment has been assessed by applying the generalized multireference analogue of the Davidson correction [27,28] to the extrapolated $T = 0$ energies of each root.

The next step in the LSC–SO–CI approach is a spin–orbit CI in a basis of the Λ–S eigenfunctions multiplied with appropriate spin functions. The estimated full CI energies are placed on the diagonal of the Hamiltonian whereas the variational Λ–S wavefunctions are employed to calculate spin–orbit matrix elements. The secular equations thus defined are of order 67 and include as basis functions all Λ–S states converging to the four lowest PbLi dissociation limits, $\mathrm{Pb}(^3P, ^1D, ^1S) + \mathrm{Li}(^2S)$ and $\mathrm{Pb}(^3P) + \mathrm{Li}(^2P)$, as well as a number of higher-lying states. The final Ω wavefunctions are employed to compute various properties such as electric dipole and transition moments, which are used to obtain Einstein coefficients and radiative lifetimes for excited states. Results are calculated for a large range of internuclear distances from $r = 3.0$ to $7.5a_0$ in steps of $0.1a_0$ and at selected points for larger separations up to $15.0a_0$. In the more flexible MR–SO–CI treatment, calculations are carried out for all symmetry-adapted functions (SAFs) selected for the various Λ–S spaces at $T = 1.0 \times 10^{-6} E_h$. Near the PbLi $X^4\Sigma^-$ equilibrium distance ($r = 5.0a_0$) the resulting secular equation is of order 85 175, from which the lowest seven roots have been calculated, similarly as at all other distances treated.

The potential curves obtained for the PbLi system without inclusion of the spin–orbit interaction are shown in Fig. 9. It can be seen that, in contrast to the PbH and PbF systems, the PbLi radical has numerous bound Λ–S states in the low-energy excitation range. The PbLi ground state is calculated to be $^4\Sigma^-(\ldots\sigma\pi^2)$, once again different from the $^2\Pi(\ldots\sigma^2\pi)$ ground state characteristic for PbH and PbF. An explanation for the above findings is fairly simple. The σ orbital in PbLi is not so strongly bound as in PbF or PbH, while the highest occupied π orbital acquires some slight bonding character in this system, being completely localized on the Pb atom in PbH and PbF. The above result is very

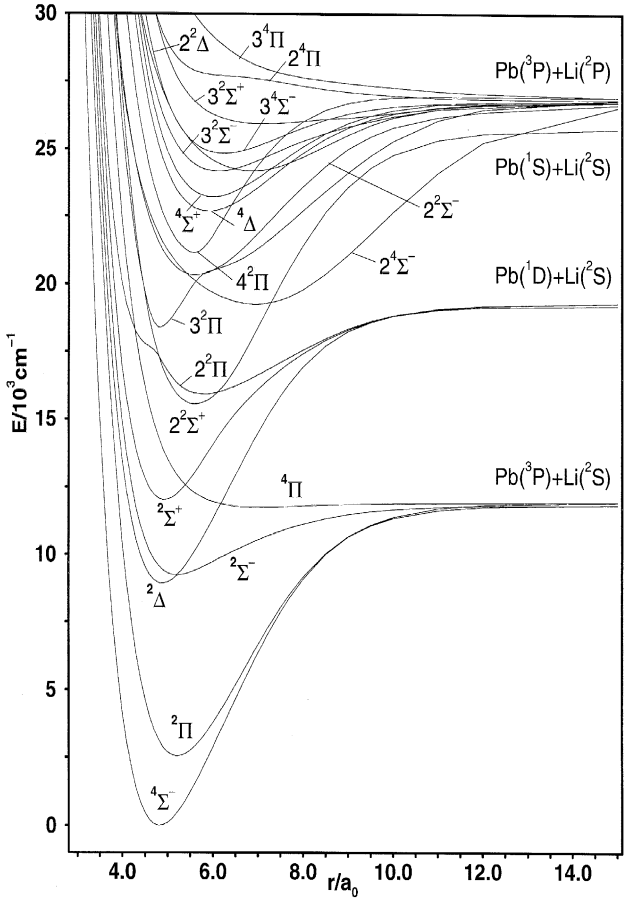

Fig. 9. Computed potential energy curves of the low-lying Λ–*S* states of PbLi obtained without inclusion of the spin–orbit interaction.

important, because it means that much less energy is required for the $\sigma \rightarrow \pi$ excitation in PbLi. Therefore, it becomes energetically advantageous to form the $^4\Sigma^-(\ldots\sigma\pi^2)$ ground state, with all three outer electrons having parallel spins, than the lower multiplicity $^2\Pi(\ldots\sigma^2\pi)$ state. The ground state bonding energy in PbLi is much smaller (≈1.6 eV calculated at the Λ–*S* level) than in PbH (≈2.5 eV) or PbF (≈4.3 eV), however. It is closely followed by the $^2\Pi(\ldots\sigma^2\pi)$ state, with an excitation energy of only 0.35 eV computed without including the spin–orbit interaction. Three other electronic states, $^2\Delta, ^2\Sigma^-$, and $^2\Sigma^+$, arising from the same $\ldots\sigma\pi^2$ configuration as $X^4\Sigma^-$, have fairly low excitation energies and are bound as well, for to the same reasons as discussed above. Moreover, the counterpart of the σ binding orbital, σ^*, is relatively weakly repulsive and this leads to the bound character of states resulting from the $\sigma, \pi \rightarrow \sigma^*$ excitations, as $2^2\Sigma^+(\ldots\sigma^2\sigma^*)$, $2^2\Pi(\ldots\sigma\pi\sigma^*)$, $2^2\Sigma^-(\ldots\pi^2\sigma^*)$, and $2^4\Sigma^-(\ldots\pi^2\sigma^*)$. There are numerous other low-lying excited states in the PbLi radical, such as $3^2\Pi(\ldots\pi^3)$, $4^2\Pi(\ldots\sigma\pi\sigma^*)$, $1^4\Delta(\ldots\sigma\pi\pi^*)$, $1^4\Sigma^+(\ldots\sigma\pi\pi^*)$, $2^2\Delta(\ldots\pi^2\sigma^*)$, and $3^2\Sigma^-(\ldots\sigma\pi^*)$, and they are all bound, thus producing a very complex low-energy electronic structure for PbLi. It becomes even more complicated when the spin–orbit interaction is taken into account.

Addition of the spin–orbit coupling gives the Ω-state potential curves shown in Figs. 10 and 11 for the LSC–SO–CI and MR–SO–CI approaches, respectively. One can see that for the lowest seven states the two sets of potential energy curves agree quite well qualitatively, though there are some quantitative distinctions, in particular in the excitation energies. The most important difference appears for the *B* and *C* states, and this will be discussed in more detail in the following section.

The $X^4\Sigma^-$ state is split into the X_1 1/2 and X_2 3/2 components. The zero-field splitting computed by employing the LSC–SO–CI approach is 1602 cm^{-1} and thus much smaller than for the corresponding X_1 and X_2 states in PbH or PbF, characterized by the $\Delta E(X_2 - X_1)$ values of 7000 and 8264 cm^{-1}, respectively. This finding is easy to understand, because the X_1 and X_2 states of PbLi originate predominantly from the $X^4\Sigma^-$ state ($\Lambda = 0$) and therefore the splitting is a second-order effect, in contrast to the first-order splitting of the $X^2\Pi$

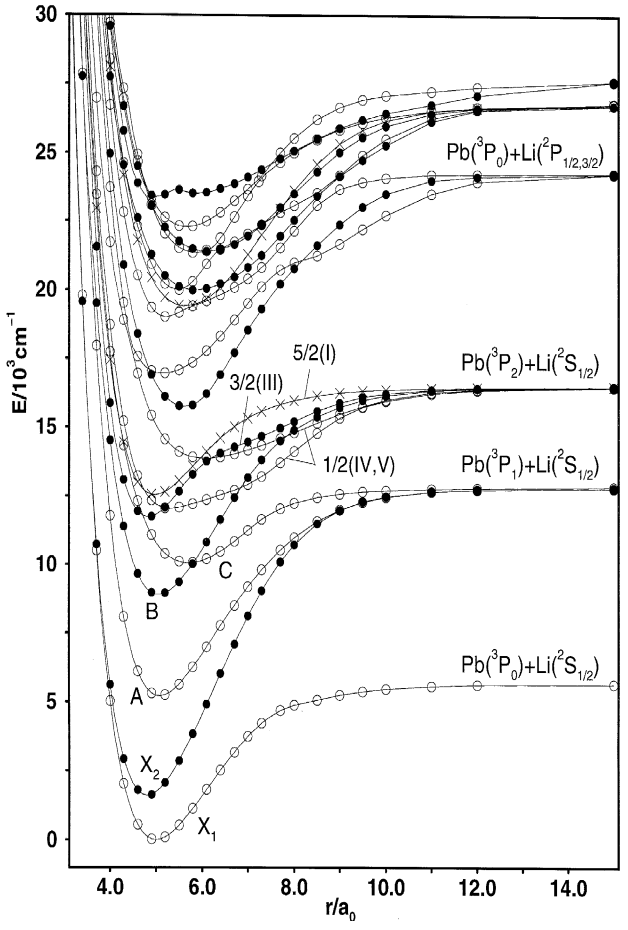

Fig. 10. Computed potential energy curves for the low-lying Ω states of PbLi obtained in the LSC–SO–CI approach: ○, $\Omega = 1/2$ states; ●, $\Omega = 3/2$ states; and ×, $\Omega = 5/2$ state.

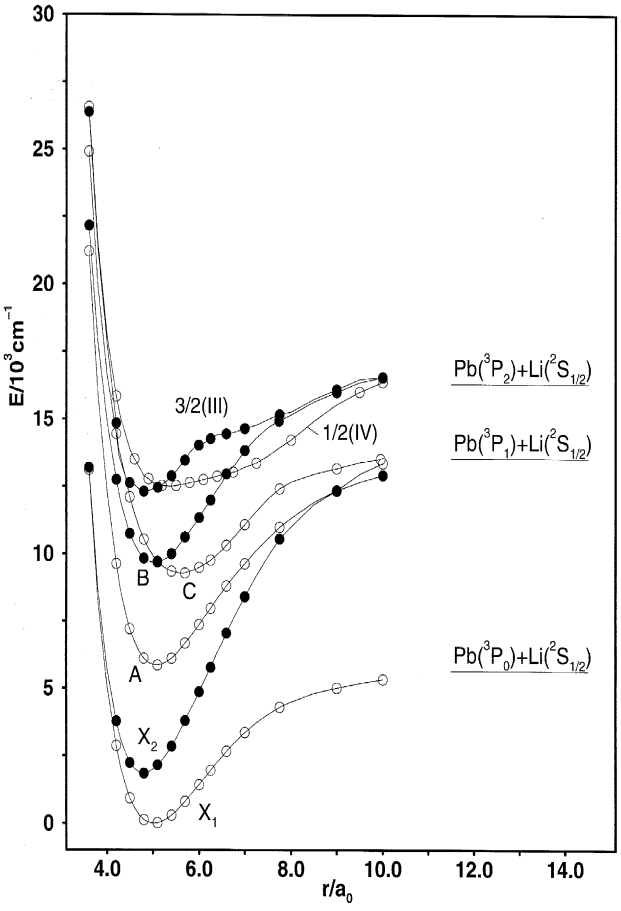

Fig. 11. Computed potential energy curves for the seven lowest Ω states of PbLi obtained in the MR–SO–CI approach: ○, $\Omega = 1/2$ states and ●, $\Omega = 3/2$ states.

state in PbH and PbF. The ground state splitting is mainly caused by the $X^4\Sigma^- - 1^2\Pi$ spin–orbit interaction, although contributions from the $1^2\Sigma^+$, $1^2\Sigma^-$, and $1^2\,\Delta$ states are also not negligible. The upper X_2 3/2 component is characterized by a notably larger vibrational frequency than X_1, mainly by virtue of the fact that it converges to the $\mathrm{Pb}(^3P_1) + \mathrm{Li}(^2S)$ dissociation limit, lying significantly (by 7819 cm^{-1}) higher than the lowest $\mathrm{Pb}(^3P_0) + \mathrm{Li}(^2S)$ limit.

The second excited state of the PbLi system, A 1/2, is calculated to lie at 5211 cm^{-1} above the X_1 ground state. It is almost a 50/50 mixture of the $X^4\Sigma^-$ and $1^2\Pi$ Λ–S states at the X_1 equilibrium distance and it is characterized by ω_e and r_e values very similar to those of the X_1 state. There is some alternation of the $\Omega = 1/2$ and 3/2 states in the low-energy PbLi spectrum, with B 3/2 appearing as next in energy, at 8891 cm^{-1}. Near its potential minimum, it has a 50% contribution from the $1^2\Pi$ state, with an additional 50% coming from $1^2\Delta$ (≈30%), $X^4\Sigma^-$ (≈16%) and a number of minor admixtures. Once again, the ω_e and r_e values for this state do not differ significantly from the corresponding X_1 spectroscopic constants.

The situation is different for the next excited state, C 1/2, which has a minimum shifted quite strongly to longer distances. The reason for this is its predominantly $1^4\Pi$ composition (59% at $r_e^C \approx 5.7a_0$), with this Λ–S state possessing a very flat potential curve with a minimum of only 215 cm^{-1} (see Fig. 9). The much deeper minimum in the final C 1/2 potential results from the strong $1^4\Pi$ first-order spin–orbit splitting as well as from its coupling with other Λ–S states, such as $1^2\Pi$ (4.1%), $2^2\Pi$ (7.2%), $2^2\Sigma^+$ (9.2%), $1^2\Sigma^-$(8.1%), $X^4\Sigma^-$ (5.1%), etc. One can see that the Λ–S composition becomes quite complicated for the PbLi excited states and that it changes quite fast with internuclear distance. This is an important consideration which should be kept in mind during analysis of the corresponding radiative transitions.

At an excitation energy of approximately 11750 cm^{-1} one finds the 3/2(III) state, which has not yet been identified experimentally and therefore does not have any letter notation. It is dominated by the $1^2\Delta$ contribution (approx 48%), but admixtures of $1,3^2\Pi$, $2^4\Sigma^-$, and $1^4\Pi$ are also important. The 1/2(IV) state lies only 300 cm^{-1} above 3/2(III) and is mainly $1^2\Sigma^-$ in origin in the Franck–Condon region. This explains the shape of the 1/2(IV) potential curve (compare Figs. 9 and 10), although contributions from the other Λ–S states have a fairly strong influence. The only $\Omega = 5/2$ state in the low-energy PbLi spectrum comes primarily from the $1^2\Delta$ state (≈75%) and is calculated to lie at energy of ≅12500 cm^{-1}. It is closely followed by the 1/2(V) state (predominantly $1^4\Pi$), which is characterized by a rather flat potential curve very much shifted to longer distances.

We have already analyzed nine electronic states and it should be underlined that all of them are bound and lie within 14 000 cm^{-1} above the ground state. This shows that experimental analysis and assignment of the observed luminescence spectra should be by no means a trivial task. An additional complication is caused by the strong spin–orbit coupling characteristics of the PbLi system, which cause the significantly mixed final Ω electronic states. This makes radiative transitions for almost all combinations of the above states allowed and of comparable strength. Therefore the calculated spectroscopic parameters (T_e, ω_e, and r_e), transition moments and radiative lifetimes should be very helpful for identification of the emission spectra, and such an analysis will be carried out in the next section.

5. Discussion

A summary of spectroscopic constants measured in the present study is given in Table 6 in comparison with the calculated results obtained with both computational approaches described in the previous section. The X_2–X_1

Table 6
Spectroscopic constants of $^{208}Pb^{7}Li$ and comparison of experimental results with theoretical predictions

	T_e (cm^{-1})		ω_e (cm^{-1})		r_e (Å)	
	Experimental	Theoretical	Experimental	Theoretical	Experimental	Theoretical
X_1 1/2	0	0	309.2	312	2.704	2.644
				(305)[a]		−2.654
X_2 3/2	2086.6	1602		368		2.545
		(1851)		(370)		(2.539)
A 1/2	6058.5	5211	319.8	328	2.717	2.686
		(5867)		(325)		(2.684)
B 3/2	8933.2	8891	323.0	325	2.680	2.672
		(9678)		(321)		(2.661)
C 1/2	9974.1	10044	195.7	205		3.015
		(9297)		(222)		(2.962)
3/2(III)		11741		344		2.557
1/2(IV)		12054		202		2.809
5/2(I)		12534		309		2.631
1/2(V)		13872		140		3.204
3/2(IV)		15735		278		2.962
1/2(VI)		16959		215		2.722

[a] Theoretical values without parentheses are LSC–SO–CI results, values in parentheses are calculated in the MR–SO–CI approach.

fine-structure splitting is measured to be 2086.6 cm^{-1}, whereas the corresponding values for PbH and PbF are almost four times larger. The present calculations give a value of 1602 cm^{-1} in the LSC–SO–CI treatment and 1851 cm^{-1} in MR–SO–CI. The latter result agrees better with experiment and there are additional theoretical grounds to believe that it is more accurate. One can show that the lowest $\Omega = 1/2$ states in PbLi require for their description spin–orbit coupling involving high-lying virtual MOs because of their importance for obtaining accurate Pb $6p_{1/2}$ spin–orbitals, which have higher partial weight in the 1/2 states. Such contributions are not adequately included in the LSC–SO–CI treatment on the whole, because they do not play an important role in the limited number of the Λ–S states taken into account in this approach. The influence of high-energy excitations on the 3/2 states is weaker and this may lead to some underestimation of the 3/2–1/2 splitting for the PbLi ground state. The same effect has also been found in the analogous PbF calculations [20]. This problem in general has been analyzed in more detail in our earlier study [23].

Vibrational frequency values for the X_1 state calculated by the two different methods differ by only 7 cm^{-1} and agree quite well with the experimental result, which lies in between them. Both computed r_e values are smaller (by 0.05–0.06 Å) than the measured bond distances. The present calculations indicate that the X_2 state is characterized by a notably shorter equilibrium distance than X_1. This is caused by the strong spin–orbit coupling of X_1 with the closely lying $1^2\Pi_{1/2}$ state, which leads to a significant lengthening of the corresponding bond, from 2.550 Å calculated at the Λ–S level to 2.644 Å. The analogous effect for the upper X_2 3/2 component is much weaker due to a strong $1^2\Pi$ internal splitting (5530 cm^{-1} at $r = 5.5a_0$). Unfortunately, it was not possible to determine an accurate experimental r_e (X_2) value, but the above theoretical trend is confirmed by the good agreement of the experimental band profiles of the $A \rightarrow X_2$ and $B \rightarrow X_2$ transitions with simulated contours obtained when the $B_0(X_2)$ value is derived from the theoretical $r_e(X_2)$ result (Figs. 6 and 7). There is little hope to observe the X_2–X_1 transition experimentally due to its very low excitation energy and fairly small transition moment (see Fig. 12). The calculated radiative lifetime of X_2, $v = 0$ is extremely long: 4.5 s.

The next lowest electronic state is A 1/2, with a measured T_0 excitation energy of 6058.5 cm^{-1}. The LSC–SO–CI approach gives a notably lower T_e value of 5211 cm^{-1}, whereas 5867 cm^{-1} is obtained in the MR–SO–CI calculations, in much better agreement with experiment. As can be seen from Table 6, the agreement between the experimental and computed ω_e and r_e parameters is quite good. Dipole moments computed for transitions from the A state to the X_2 and X_1 states are shown in the lower panel of Fig. 13. While perpendicular transitions to X_2 and X_1 are fairly weak, the parallel $A \rightarrow X_1$ transition is much stronger and shows a significant dependence on internuclear distance. This transition borrows its intensity mainly from the strong $X^4\Sigma^- - 1^2\Pi$ spin–orbit mixing and thus is proportional to the dipole moment difference for the corresponding Λ–S states, which is relatively large in this case, 0.815 ea_0. The calculated radiative lifetime for the parallel A, $v' = 0 \rightarrow X_1$ transition is 17.5 μs, while two possible perpendicular transitions are characterized by τ values approximately 100 times longer (see Table 7). These results are in good agreement with the experimentally observed intensity ratio of the $A \rightarrow X_1$ and $A \rightarrow X_2$ bands of ≈150.

The B 3/2 state is determined experimentally to lie at $T_0 = 8933.2$ cm^{-1}, while the LSC–SO–CI calculated

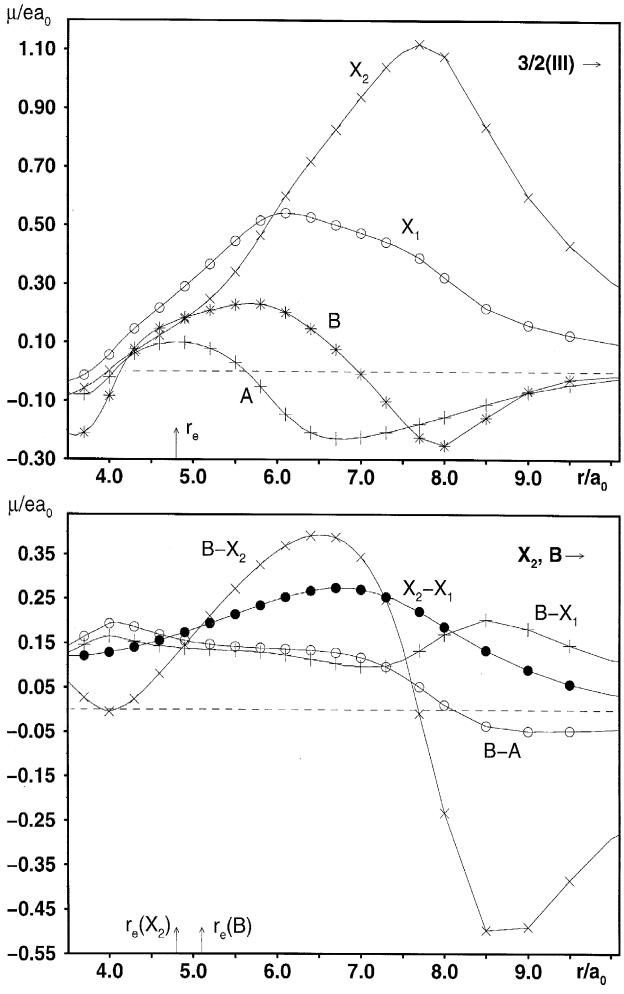

Fig. 12. Computed electric dipole moments for transitions from the X_2, B (lower panel) and 3/2(III) (upper panel) states to the lower-lying states of PbLi.

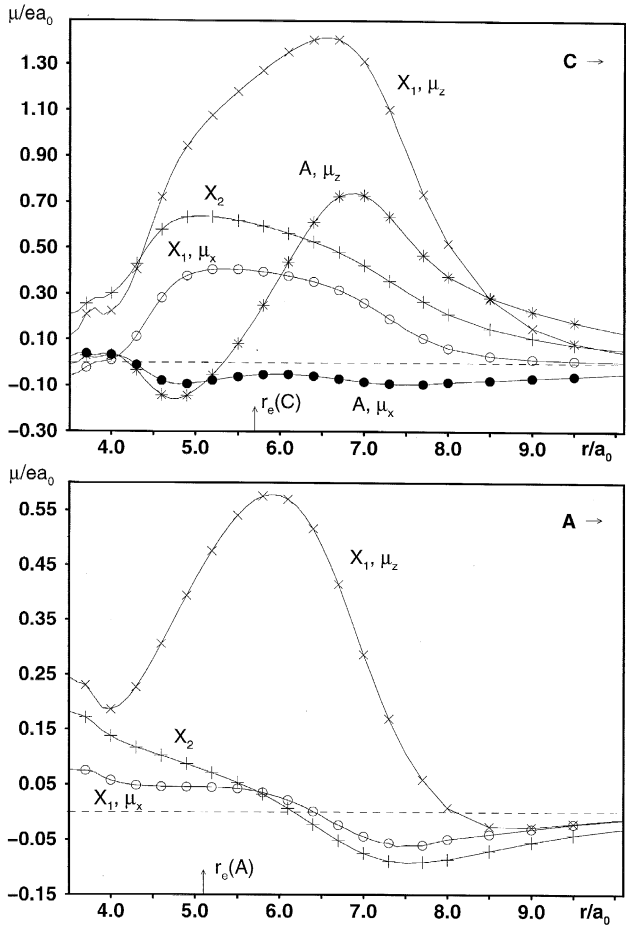

Fig. 13. Computed electric dipole moments for transitions from the A (lower panel) and C (upper panel) $\Omega = 1/2$ states to the lower-lying states of PbLi. The $\mu_{z,x}$ notation corresponds to the parallel and perpendicular transitions, respectively.

result is 8891 cm^{-1}. Such excellent agreement may be at least partly due to cancellation of errors. The MR–SO–CI calculations predict the B state excitation energy to be almost 700 cm^{-1} higher. Although such accuracy is still acceptable given the complicated PbLi electronic structure, it can be noted that the MR–SO–CI results become somewhat less accurate for the higher-lying excited states. This may be caused by some deficiency of the CI treatment in the MR–SO–CI method as compared to LSC–SO–CI, since the need to diagonalize full SO–CI matrices in the former case compelled us to use a higher selection threshold than in the LSC–SO–CI calculations (1.0 vs. 0.05 μ_H), and no $T \to 0$ extrapolation and full-CI correction have been used. This aspect may become more critical for the higher-lying states. The ω_e and r_e values obtained in both types of calculations agree very well (within 1–2%) with each other and with the experimental results, however, which shows that shapes of the potential energy curves (Figs. 10 and 11) are described well in both approaches. The calculated transition moments for the $B \to X_1, X_2$ transitions are approximately equal at $r_e(B)$ (see Fig. 12) and this leads to very similar τ ($v' = 0$) values of approximately 40 μs for both transitions. Experimentally, the $B \to X_2$ band at 6851 cm^{-1} (Fig. 7) is found to be at least a factor of 10 weaker than the $B \to X_1$ band at 8930 cm^{-1} (Fig. 2). The reason for this discrepancy most likely lies in the different behaviour of the $\mu(B \to X_1, X_2)$ quantities as a function of internuclear distance (see Fig. 12). The $\mu(B \to X_1)$ transition moment remains almost constant near the $r_e(B)$ equilibrium distance, while $\mu(B \to X_2)$ changes quite fast in this range. A small shift of the $\mu(B \to X_2)$ curve to larger distances (we slightly underestimate the $r_e(X_1, X_2, B)$ values) would lead to a notable change of the $B \to X_1/B \to X_2$ intensity ratio in favour of the $B \to X_1$ transition.

The next excited state, C 1/2, is observed about 1000 cm^{-1} higher than B 3/2, at $T_0 = 9974.1\ cm^{-1}$. The LSC–SO–CI method predicts an excitation energy for this state of 10 044 cm^{-1}, while the MR–SO–CI approach gives a notably smaller value of 9297 cm^{-1}. This

Table 7
Calculated partial radiative lifetimes τ(s) for the low-lying states of $^{208}Pb^{7}Li$ ($v' = 0$)

State	X_2 3/2	A 1/2	B 3/2	C 1/2	3/2(III)	1/2(IV)	5/2(I)	1/2(V)[a]	3/2(IV)[a]	1/2(VI)[a]
X_1 1/2	4.5 (0)	1.7(−3) x[b]	37.9(−6)	4.1(−6) x	3.82(−6)	1.83(−6) x		8.5(−6) x	5.9(−6)	6.8(−6) x
		17.5(−6) z		0.42(−6) z		0.54(−6) z		45(−6) z		0.52(−6) z
X_2 3/2		2.1(−3)	41.7(−6)	4.68(−6)	15.7(−6)	105(−6)	9.8(−6)	24.5(−6)	2.2(−6)	92.8(−6)
A 1/2			440(−6)	2.3(−3) x	211(−6)	407(−6) x		14.1(−6) x	2.4(−6)	2.0(−6) x
				4.7(−6) z		22.1(−6) z		105(−6) z		0.27(−6) z
B 3/2					740(−6)	530(−6)	5.0(−3)	290(−6)	310(−6)	8.1(−6)
C 1/2						2.9(−3) x		3.0(−3) x	2.7(0)	30.2(−6) x
						81.0(−6) z		570(−6) z		50.3(−6) z
3/2(III)							0.23(0)		9.7(−6)	54.1(−6)
1/2(IV)								8.4(−3) x	3.0(−3)	160(−6) x
								106(−6) z		1.1(−3) z

[a] Radiative lifetime values for this state are estimated for its equilibrium distance.
[b] x and z correspond to perpendicular and parallel transitions, respectively.

means that according to the MR–SO–CI calculations C 1/2 lies lower than B 3/2 (see Fig. 11), and this is in a clear contradiction to the experimental data. In contrast, the LSC–SO–CI calculations give not only the correct ordering of the B and C states, but also predict their excitation energies with fairly high accuracy. The vibrational frequency for the C state, calculated by the LSC–SO–CI method to be 205 cm^{-1}, also agrees better with the experimental value of 195.7 cm^{-1}. It can be noted, however, that, as in the B state case, both theoretical methods are in fairly good agreement with each other for the shape of the C potential curve (see Figs. 10 and 11). It is predicted to be strongly shifted to longer distances as compared to the X_1 ground state and to be characterized by a much lower vibrational frequency. Altogether, one can conclude that the LSC–SO–CI method provides more accurate calculated data for the C 1/2 state, which, as in the case of B 3/2, most probably can be explained by the higher level of the correlation treatment in the Λ–S contracted approach.

As has already been discussed in the previous section, the largest Λ–S contribution for the C state near its equilibrium distance comes from the $1^4\Pi$ state. Since the X_1 and X_2 states are mainly $^4\Sigma^-$ in character, one would expect that perpendicular transitions dominate the C emission spectrum. One can see from Fig. 13 and Table 7, however, that this is not true and that the strongest transition is the parallel $C \rightarrow X_1$. It is characterized by a radiative lifetime of 0.42 μs and is thus roughly 10 times stronger than the $C \rightarrow X_2$, A transitions, which is in line with the experimental findings. A detailed analysis shows that a strong admixture of the $1^2\Pi$ character to both the X_1 and C states, as well as fairly large contributions of $1^4\Pi$ for the X_1 wavefunction and of $1^4\Sigma^-$ for C are responsible for this effect. This result underlines once again the influence of the complicated Λ–S composition of the final Ω states on their radiative properties. Among the five experimentally observed C, $v' = 0 \rightarrow X_1$, $v'' = 1$–5 bands, 0–3 is found to be the strongest, which is easily explained because of the notably larger bond length of the upper state. This trend is confirmed by the present calculations, which give Einstein coefficients of 0.578, 0.607, and $0.434 \times 10^6\ s^{-1}$ for the 0–2, 0–3, and 0–4 bands, respectively.

No other electronic states have as yet been identified in the PbLi spectrum. The potential curves presented in Fig. 10 indicate that in addition to the lowest states already discussed, there are 14 more states with excitation energy below 3 eV, and all of them are bound. The calculated radiative lifetimes for the six lowest states of this group are given in Table 7. It can be seen that they all have τ values in the 0.1–10 μs range, so that it should not be technically difficult to observe them. Some problems may arise in their assignment, however, due to the high density of states in this energy range [(12–24) $10^3\ cm^{-1}$], similar values of transition moments and possible nonadiabatic processes. In the present study, we have concentrated on the five lowest electronic states, however.

The J-independent "hyperfine doubling" observed for the $A \rightarrow X_1$ lines of $^{207}Pb^{7}Li$ is a characteristic of $^1\Pi$ and $^2\Pi_{1/2}$ states [17]. It is caused by interaction of the nuclear spin $I = 1/2$ of ^{207}Pb with the spin of an unpaired π electron of the $\ldots\sigma^2\pi$ configuration and is expected to approach the hfs splitting in the $6p\ ^2P_{1/2}$ state of $^{207}Pb^+$ if the π electron is localized on the Pb atom. Such a case has been found in the $X_1{}^2\Pi_{1/2}$ state of ^{207}PbF [15]. The value of the splitting parameter $d = 0.244\ cm^{-1}$ observed in the present work is nearly identical to the value $|d| = 0.242\ cm^{-1}$ found in ^{207}PbF [15]. This suggests that the splitting is a characteristic of the A 1/2 state and that this state is mostly $^2\Pi_{1/2}$ in nature, arising from the $\ldots\sigma^2\pi$ configuration with the π electron located at the Pb atom. However, whereas calculations showed that these conditions are nearly fulfilled for the $X_1{}^2\Pi_{1/2}$ state of ^{207}PbF, in $^{207}Pb^{7}Li$ the X_1 1/2 and A 1/2 states definitely are nearly perfect 1:1 mixtures of the $X^4\Sigma^-$ and $1^2\Pi$ Λ–S states at the X_1 equilibrium distance. Therefore, the hfs splitting should be nearly the same in both states and should cancel for

the P and R lines of the $A \rightarrow X_1$ transition. Furthermore, the hfs splitting in the X_1 1/2 state should show up in the B 3/2$\rightarrow X_1$ 1/2 lines of ^{207}Pb^{7}Li, which has not been observed. Partial cancellation of the hfs splitting effects due to strong spin–orbit mixing of the states has recently been observed in the $A_2{}^4\Pi_{1/2} \rightarrow X_1{}^2\Pi_{1/2}$ transition of BiO [29]. More experimental and theoretical work is needed to solve these problems.

Acknowledgments

Financial support of this work by the Deutsche Forschungsgemeinschaft and the Fonds der Chemischen Industrie is gratefully acknowledged. J. B.-B.,W.Z. and A.M.P. would like to thank the Deutsche Forschungsgemeinschaft for financial support during their stay in Wuppertal.

References

[1] K.P. Huber, G. Herzberg, Molecular Spectra and Molecular Structure, vol. 4, Constants of Diatomic Molecules, Van Nostrand-Reinhold, New York, 1979.
[2] P.F. Bernath, S. McLeod, J. Mol. Spectrosc. 207 (2001) 287.
[3] K.D. Setzer, C. Uibel, W. Zyrnicki, A.M. Pravilov, E.H. Fink, H.-P. Liebermann, A.B. Alekseyev, R.J. Buenker, J. Mol. Spectrosc. 204 (2000) 163–175.
[4] K.D. Setzer, E.H. Fink, A.B. Alekseyev, H.-P. Liebermann, R.J. Buenker, J. Mol. Spectrosc. 206 (2001) 181–197.
[5] A. Mavridis, J.F. Harrison, J. Phys. Chem. 86 (1982) 1979–1985.
[6] A. Mavridis, J.F. Harrison, J.F. Liebman, J. Phys. Chem. 88 (1984) 4973–4978.
[7] A.I. Boldyrev, J. Simons, P.v.R. Schleyer, J. Chem. Phys. 99 (1993) 8793–8804.
[8] A.I. Boldyrev, J. Simons, J. Phys. Chem. 97 (1993) 1526–1532.
[9] A.I. Boldyrev, N. Gonzales, J. Simons, J. Phys. Chem. 98 (1994) 9931–9944.
[10] A. Ricca, C.W. Bauschlicher Jr., Chem. Phys. Lett. 244 (1995) 32–38.
[11] F.B.C. Machado, R. Bravo, O. Roberto-Neto, J. Mol. Struct. (THEOCHEM) 464 (1999) 7–14.
[12] J. Xin, L.M. Ziurys, J. Chem. Phys. 110 (1999) 4797–4802.
[13] V. Kaufman, B. Edlén, J. Phys. Chem. Ref. Data 3 (1974) 825–895.
[14] K.D. Setzer, J. Borkowska-Burnecka, W. Zyrnicki, E.H. Fink, J. Mol. Spectrosc. 203 (2000) 244–248.
[15] K. Ziebarth, K.D. Setzer, E.H. Fink, J. Mol. Spectrosc. 191 (1998) 108–116.
[16] K.D. Setzer, J. Borkowska-Burnecka, W. Zyrnicki, E.H. Fink (to be published).
[17] C.H. Townes, A.L. Schawlow, Microwave Spectroscopy, Dover, New York, 1975.
[18] D.J.W. Lumley, R.F. Barrow, J. Phys. B 10 (1977) 1537–1541.
[19] S.A. Wildman, G.A. DiLabio, P.A. Christiansen, J. Chem. Phys. 107 (1987) 9975–9979.
[20] K.K. Das, I.D. Petsalakis, H.-P. Liebermann, A.B. Alekseyev, R.J. Buenker, J. Chem. Phys. 116 (2002) 608–616.
[21] L.F. Pacios, P.A. Christiansen, J. Chem. Phys. 82 (1985) 2664–2671.
[22] A.B. Alekseyev, H.-P. Liebermann, R.J. Buenker, G. Hirsch, Y. Li, J. Chem. Phys. 100 (1994) 8956–8968.
[23] R.J. Buenker, A.B. Alekseyev, H.-P. Liebermann, R. Lingott, G. Hirsch, J. Chem. Phys. 108 (1998) 3400–3408.
[24] R.J. Buenker, S.D. Peyerimhoff, Theor. Chim. Acta 35 (1974) 33–58;
Theor. Chim. Acta 39 (1975) 217–228;
R.J. Buenker, S.D. Peyerimhoff, W. Butscher, Mol. Phys. 35 (1978) 771–791.
[25] R.J. Buenker, R.A. Philips, J. Mol. Struct. (THEOCHEM) 123 (1985) 291–300.
[26] S. Krebs, R.J. Buenker, J. Chem. Phys. 103 (1995) 5613–5629.
[27] E.R. Davidson, in: R. Daudel, B. Pullman (Eds.), The World of Quantum Chemistry, Reidel, Dordrecht, 1974, p. 17.
[28] G. Hirsch, P.J. Bruna, S.D. Peyerimhoff, R.J. Buenker, Chem. Phys. Lett. 52 (1977) 442–448;
D.B. Knowles, J.R. Alvarez-Collado, G. Hirsch, R.J. Buenker, J. Chem. Phys. 92 (1990) 585–596.
[29] O. Shestakov, R. Breidohr, H. Demes, K.D. Setzer, E.H. Fink, J. Mol. Spectrosc. 190 (1998) 28–77.